






Imaging Threading Dislocations and Surface Steps in Nitride Thin Films Using Electron Backscatter Diffraction

Kieran P. Hiller¹ , Aimo Winkelmann^{1,2} , Ben Hourahine¹ , Bohdan Starosta¹,
Aeshah Alasmari¹, Peng Feng³, Tao Wang³, Peter J. Parbrook⁴, Vitaly Z. Zubialeovich⁴,
Sylvia Hagedorn⁵, Sebastian Walde⁵, Markus Weyers⁵, Pierre-Marie Coulon^{6,7}, Philip A. Shields⁶,
Jochen Bruckbauer^{1,*} , and Carol Trager-Cowan¹ 

¹Advanced Materials Diffraction Lab, Department of Physics, SUPA, University of Strathclyde, Glasgow G4 0NG, UK

²Academic Centre for Materials and Nanotechnology, AGH University of Krakow, Kraków 30-055, Poland

³Department of Electronic and Electrical Engineering, University of Sheffield, Sheffield S1 3JD, UK

⁴Tyndall National Institute, University College Cork, Cork T12 R5CP, Ireland

⁵Ferdinand-Braun-Institut, Leibniz-Institut für Höchstfrequenztechnik, D-12489 Berlin, Germany

⁶Department of Electronic and Electrical Engineering, University of Bath, Bath BA2 7AY, UK

⁷CNRS-CRHEA, Université Côte d'Azur, 06560 Valbonne, France

*Corresponding author: Jochen Bruckbauer, E-mail: jochen.bruckbauer@strath.ac.uk

Abstract

Extended defects, like threading dislocations, are detrimental to the performance of optoelectronic devices. In the scanning electron microscope, dislocations are traditionally imaged using diodes to monitor changes in backscattered electron intensity as the electron beam is scanned over the sample, with the sample positioned so the electron beam is at, or close to the Bragg angle for a crystal plane/planes. Here, we use a pixelated detector instead of single diodes, specifically an electron backscatter diffraction (EBSD) detector. We present postprocessing techniques to extract images of dislocations and surface steps, for a nitride thin film, from measurements of backscattered electron intensities and intensity distributions in unprocessed EBSD patterns. In virtual diode (VD) imaging, the backscattered electron intensity is monitored for a selected segment of the unprocessed EBSD patterns. In center of mass (COM) imaging, the position of the center of the backscattered electron intensity distribution is monitored. Additionally, both methods can be combined (VDCOM). Using both VD and VDCOM, images of only threading dislocations, or dislocations and surface steps can be produced, with VDCOM images exhibiting better signal-to-noise. The applicability of VDCOM imaging is demonstrated across a range of nitride semiconductor thin films, with varying surface step and dislocation densities.

Key words: SEM, nitrides, thin film semiconductors, extended defects, dislocations, EBSD

Introduction

It is known that the presence of threading dislocations in group III-nitride semiconductors inhibits the performance of (opto) electronic devices (Wu et al., 1996; Mathis et al., 2001; Nagahama et al., 2001). Due to the growth on foreign substrates, such as sapphire and silicon, these materials exhibit relatively large densities of threading dislocations of the order of 10^8 – 10^9 cm⁻². Generally, threading dislocations in nitrides are centers for nonradiative recombination; however, there is still ambiguity in the literature on the effect of dislocation types on the optical activity (Lähmann et al., 2022). Dislocations are the cause of leakage currents, decreased device efficiencies, limited lifetimes in visible InGaN/GaN-based light emitting diodes (LEDs) and ultraviolet AlGaIn-based LEDs (Kneissl et al., 2019; Weisbuch, 2019), reduced lifetimes of laser diodes (LDs) (Bojarska-Cieślińska et al., 2021) and decreased device performance of high electron mobility transistors (HEMTs) (Setera & Christou, 2021). Therefore, investigating, characterizing, and resolving dislocations plays an important role in the development of these devices; for example, investigating dislocation density,

dislocation distribution (random vs. clustering) and dislocation type.

Performing dislocation analysis for nitride semiconductors in the scanning electron microscope (SEM) has numerous benefits. Firstly, there is minimal sample preparation required. For many of the techniques performed in the SEM, samples do not have to be electron transparent, as with transmission electron microscopy (TEM). In addition to this, when imaging dislocations, the statistics are significantly greater than those in TEM cross-section measurements; i.e. one dataset simply includes a greater number of dislocations to be sampled. This is because large regions of the sample surface (e.g. 10 μm²) can be imaged in a relatively short time (of the order of minutes) with high spatial resolution.

Traditionally, in the SEM, images of dislocations have been acquired with electron channeling contrast imaging (ECCI) which uses back- and/or forescatter diodes (BSDs, FSDs) to acquire images (Wilkinson & Hirsch, 1997; Crimp et al., 2001; Trager-Cowan et al., 2007; Hite et al., 2010; Naresh-Kumar et al., 2012; Picard et al., 2012; Carnevale et al., 2014; Zaefferer & Elhami, 2014; Young et al., 2016;

Received: May 23, 2023. Revised: July 31, 2023. Accepted: September 25, 2023

© The Author(s) 2023. Published by Oxford University Press on behalf of the Microscopy Society of America.

This is an Open Access article distributed under the terms of the Creative Commons Attribution License (<https://creativecommons.org/licenses/by/4.0/>), which permits unrestricted reuse, distribution, and reproduction in any medium, provided the original work is properly cited.

Vilalta-Clemente et al., 2017; Brodusch et al., 2018; Callahan et al., 2018; Kaboli & Burnley, 2018; Miyajima et al., 2018; Schulze et al., 2018; L'hôte et al., 2019; Han et al., 2020). This is done by monitoring the change in the scalar intensity of the backscattered electron (BSE) yield as the electron beam scans continuously over the sample surface. Dislocations will be observable if the sample is placed such that the electron beam is incident on crystal planes of the sample at close to the Bragg angle, the condition for Bragg diffraction, which will influence the elastic and inelastic scattering of the incident electron beam inside the sample. In this condition, known as a “diffraction condition,” any change in crystallographic orientation or lattice constant due to strain will produce a change in the proximity to the local Bragg angle, and correspondingly a change in the BSE yield based on the diffraction effects. In ECCI images, dislocations generally appear as dots with black-white contrast.

In this study, rather than using individual hardware diodes, a pixelated detector has been utilized to image dislocations. At each point on the sample where the beam is dwelled, rather than simply collecting a scalar intensity with individual diodes, we collect an angular distribution of backscattered electrons in the form of an electron backscatter pattern (EBSP). Experimentally measured EBSPs comprise several different components. The first component is given by Kikuchi bands which represent around 10–15% of the image signal (Winkelmann et al., 2017). Kikuchi bands are formed due to the diffraction of backscattered electrons from crystal planes as they leave a crystalline sample. Kikuchi bands therefore correspond to different crystal planes and EBSPs are closely related to a 2D projection of the crystal structure. While Kikuchi bands are the basis for the quantitative analysis of orientation, crystal structure and strain in electron backscatter diffraction (EBSD) measurements (further information on this can be found in Schwartz et al., 2009), in this study it is a second component of the signal which is more important. This second component is the diffuse background of the EBSPs which is the very same signal that is monitored in ECCI measurements when using a simple diode (Nolze et al., 2017). The background component of EBSPs is smooth on the angular scales of Kikuchi diffraction effects. This is because, in the background signal, the diffraction features have been obliterated by combined, multiple elastic and inelastic scattering processes. These processes lead to mutually canceling diffraction contributions which can be assumed to originate from a distribution of effective electron sources at different energies, with reduced phase coherence, and located anywhere in the crystal unit cell (Winkelmann & Vos, 2013; Winkelmann, 2017; Winkelmann et al., 2017). Among the various self-canceling and averaging processes, the Kikuchi diffraction pattern component can be considered as a particularly stable diffraction contribution which is emphasized by the localization of quasi-elastic backscattering effects at the atomic cores on the lattice sites, in combination with a relatively narrow energy spectrum that peaks close to the primary beam energy (Winkelmann et al., 2019).

Despite the lack of direct crystallographic diffraction features in the diffuse background, the total yield and the large-scale angular distribution of the background electrons is, however, modulated by the diffraction effects of incident beam electrons, as explained previously. Figure 1 shows an as acquired EBSP (a) and the same EBSP with the diffuse background (c) removed so that only the Kikuchi bands are observed (b). A fuller explanation of the signal mechanisms involved in EBSPs is given in Schwartz et al. (2009).

A pixelated detector has much greater versatility than a diode for sample surface imaging. Firstly, the detector can be

segmented via postacquisition image processing techniques, to produce diode-like images, from anywhere across the pixel array. Here, the scalar intensity change of the BSE yield is simply monitored in specific, user-defined areas on the pixelated detector as the electron beam moves from point to point on the sample (Schwarzer & Sukkau, 2013; Nowell et al., 2014; Rampton et al., 2014; Brodusch et al., 2015; Wright et al., 2015; Nolze et al., 2017; Brodusch et al., 2018a). This method is known by various names, including virtual FSD, hybrid FSD, synthetic BSE, pattern region of interest analysis system (PRIAS) or EBSD dark field imaging mode using a virtual aperture; and we simply refer to this as virtual diode (VD) imaging here. In doing this, we are effectively moving a diode around in the SEM chamber, which means we can produce images of the same area with differing dominant contrast mechanisms (Wells et al., 1982; Wright et al., 2015; Nolze et al., 2017; Brodusch et al., 2018a; Tanaka et al., 2023). Another benefit of using a pixelated detector is that changes in the distribution of the BSE yield can be monitored in these user-defined regions. This is done by treating the intensity distribution as a mass density and monitoring the changes in the x and y positions of this mass density as the electron beam scans from point to point on the sample. This is known as center of mass (COM) imaging (Nolze et al., 2017; Winkelmann et al., 2017). VD imaging, based on the angular distribution of backscattered electrons, can also be carried out in a differential mode, by observing the relative ratio of intensities in different virtual diodes. Using three virtual diode intensity ratios, orientation color contrast can be produced from polycrystalline materials (Winkelmann et al., 2023). Moreover, for multiphase materials, where neighboring phases may have a high enough variation in electron scattering effects, large COM shifts may be measurable such that compositional changes are detectable. This could be particularly useful in geological applications of EBSD.

In this article, we present results from performing VD imaging on an N-polar GaN thin film by using a pixelated detector with the sample placed in a diffraction condition. For the same sample and diffraction condition, we then combine the VD-like detector segmentation with COM imaging, exploring the combined imaging technique of VDCOM. For both VD and VDCOM imaging, we produce separate images from the same sample area showing either threading dislocations or threading dislocations and surface steps. The underlying physics behind the signal produced in these images is discussed. The ability to controllably produce images showing both surface steps and threading dislocations allows us to identify whether threading dislocations terminate a step and therefore have a screw component or alternatively do not terminate a step and are therefore edge dislocations (Hull & Bacon, 2011). We also compare the suitability of both techniques for imaging dislocations and surface steps, where we illustrate VDCOM produces consistent signal-to-noise across both dislocation and surface step and dislocation images, whereas VD imaging does not due to signal-to-noise issues inherent in the sample-detector geometry of the experimental setup. The applicability of VDCOM imaging is then demonstrated across a range of other nitride thin films, each exhibiting different dislocation and step densities.

Materials

The N-polar GaN sample was a 900 nm thick N-polar GaN thin film grown by metal-organic vapor-phase epitaxy (MOVPE) on a sapphire substrate. The N-polar GaN was

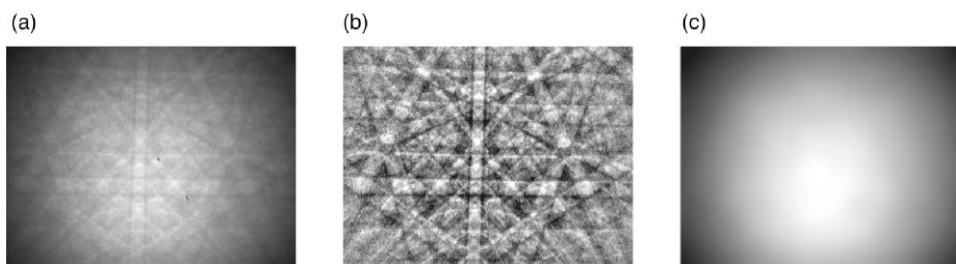


Fig. 1. (a) Raw electron backscatter pattern of a GaN thin film, acquired at 20 kV. (b) The same pattern as (a) with the diffuse background removed via a high-pass filter based on the fast Fourier Transform (FFT). (c) The diffuse background without diffraction features.

induced by high temperature (1150°C) nitridation in an environment of ammonia and H₂, followed by an estimated 25 nm thick low temperature (525°C) GaN nucleation layer and a 900 nm thick high temperature (1150°C) N-polar GaN layer.

There were two Ga-polar GaN samples used in this research. The first was a 1600 nm thick GaN thin film grown on a *c*-plane sapphire substrate via MOVPE. A 30 nm GaN nucleation layer was grown at 525°C. This layer was annealed briefly at a temperature of 1023°C prior to the epitaxial growth of the sample. More information on the growth process is available in Lafford et al. (2002). The second Ga-polar sample was a 2150 nm thick GaN thin film grown by MOVPE on a commercial AlN template from Kyma Technologies. The template consisted of a 50 nm thick nanocolumnar crystalline AlN nucleation layer grown epitaxially by plasma vapor deposition onto a sapphire substrate. The growth temperature for the GaN layer was 1060°C with H₂ as the carrier gas. TMI was used as a surfactant.

The AlN sample was a 6.6 μm thick thin film overgrown on a nanopatterned sapphire substrate (nPSS) with a miscut of 0.1° towards the sapphire *m*-plane. The overgrowth was performed in a planetary MOVPE reactor with a constant reactor pressure of 50 mbar and H₂ serving as a carrier gas. More details on the nPSS fabrication and the AlN overgrowth process can be found in Walde et al. (2020).

Methods

Acquisition

All EBSD datasets were acquired using a variable pressure field emission gun SEM (FEI Quanta 250) equipped with an Oxford Instruments Nordlys EBSD system with a sample tilt of 70°. The beam voltage for the N-polar GaN sample and AlN sample was 20 kV with a map step size of 30 and 55 nm, respectively. The beam voltage used on the other two GaN samples was 30 kV with a map step size of 25 nm. The image processing for center of mass imaging and virtual diode imaging was performed using Python. All image processing was performed on raw, as-acquired EBSPs, i.e. no diffuse background removal was used for any of the image processing techniques.

Virtual Diode Imaging

The virtual diode technique is a postacquisition image processing technique that effectively segments a pixelated detector, such as an EBSD detector, into smaller “virtual” diodes. In this case, it was performed and developed using image processing code written in Python. After collecting a full dataset of

EBSPs spanning an area of the sample, the user can define the same small region on each EBSP where the change in intensity can be monitored, going from one EBSP to the next (i.e. effectively moving across the sample). A simple example of this is as follows. A dataset contains $M \times N$ EBSPs, spanning an area on the sample surface. The EBSPs were binned down into 7×7 arrays from their original resolution of 256×336 . After doing this, a particular row was selected and the intensity within that row was summed to a single scalar value. This was performed for all EBSPs in the dataset. By then plotting each scalar value for each EBSP in the dataset in an array, a virtual diode image was obtained. The steps for this are illustrated in Figure 2. This process can be repeated for the other six rows, obtaining seven virtual diodes in total.

The value of using this virtual diode method is that we effectively move a diode up and down in the chamber and image from different locations. By doing this, we can take several images with one dataset where each image may have different features, such as crystallographic or topographical features, dominating the overall contrast. This happens because as we explore the BSE yield in different areas in the BSE distribution, we are collecting signal from different depths within the sample. The effect of how sample depth information is related to detector position is explored in Wells et al. (1982). The contrast recorded with different virtual diodes is heavily dependent on sample topography, detector-sample geometry, and electron beam voltage (Winkelmann et al., 2017).

It is important to note that VD images can be formed from an area of any size or shape, or even single pixels, in the as-acquired EBSPs. However, as the area of the EBSP sampled becomes smaller, the signal-to-noise ratio (SNR) reduces, affecting the clarity of the resulting VD images.

Center of Mass Imaging

While VD imaging monitors the changes in the intensity of the backscattered electrons incident on regions of interest on the detector, other characteristic properties of the angular distribution of the electrons on the pixelated detector can also be monitored (Chapman et al., 2016; Nolze et al., 2017; Winkelmann et al., 2017). For example, the position of the center of mass of the BSE intensity distribution (r_{COM}) is found for each EBSP using:

$$r_{\text{COM}} = \frac{1}{\sum_P I(x_p, y_p)} \begin{pmatrix} \sum_{N \times N} x_N \cdot I(x_N, y_N) \\ \sum_{M \times M} y_M \cdot I(x_M, y_M) \end{pmatrix} \quad (1)$$

Where $I(x_p, y_p)$ is the intensity measured at pixel P . The x and y coordinates of each pattern’s COM are stored in two separate arrays, one for x values and one for y values. These arrays are

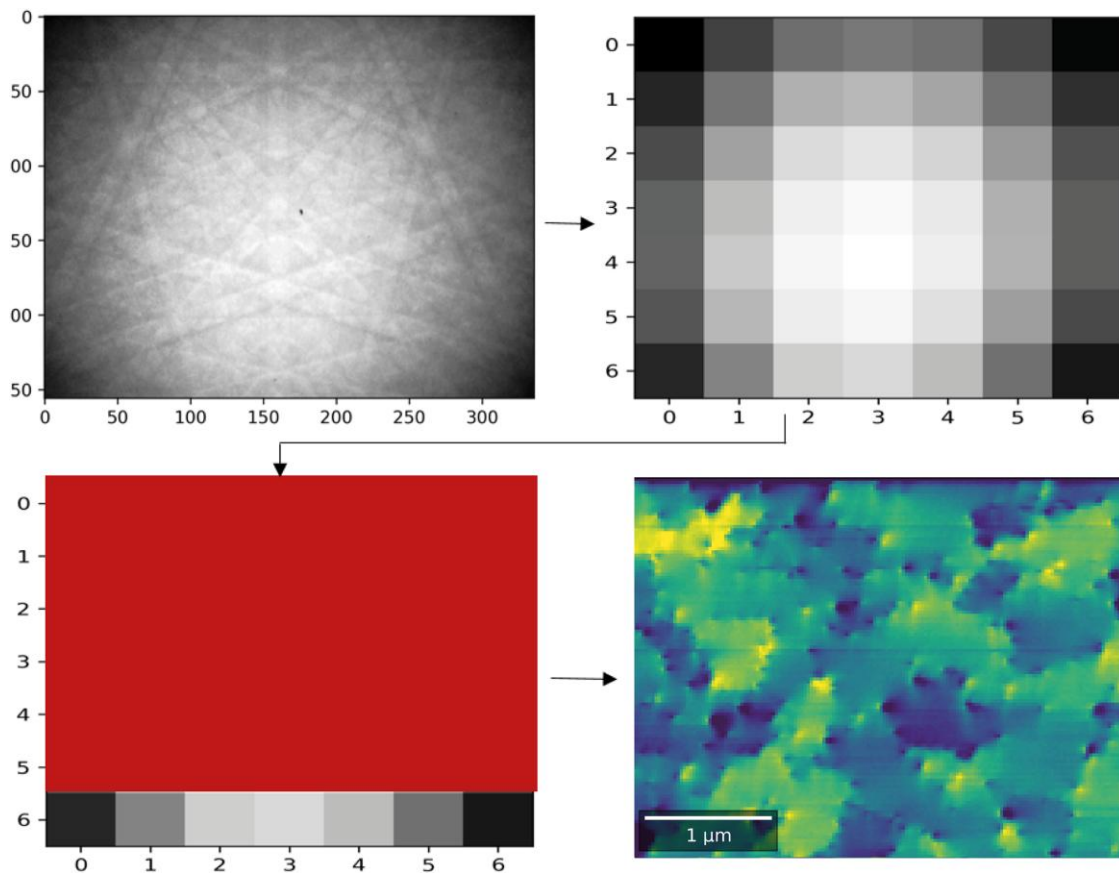


Fig. 2. Work flow of virtual diode processing method. Each EBSP in a dataset is binned into a smaller array (here 7×7). The bottom row is then chosen and the intensity is summed across the same row for all EBSPs, generating as many scalar intensity values as there are EBSPs. These values are then plotted giving a resulting image of the sample surface.

normalized by simply subtracting their mean value from each element contained in them. For a dataset with $M \times N$ EBSPs, there is then $2 \times M \times N$ values. The two separate arrays are then plotted, producing COMx and COMy images, respectively (Fig. 3).

As with VD imaging, we demonstrate here that the EBSPs can also be segmented for COM imaging (VDCOM), providing images with different dominant contrast mechanisms from one EBSD dataset. For example, COM analysis can be performed for the upper half and the lower half of each EBSP resulting in four VDCOM images. However, unlike traditional VD imaging, where binning can be high, it is important to understand that for higher binning for VDCOM imaging, smaller changes in the COM position are much less detectable. This can mean that shifts in COM images smaller than the resolution of the highly binned diodes are not detected and the resulting VDCOM images, therefore, show less contrast where a dislocation/crystal distortion is present. It is also important to note that as with VD imaging, the contrast obtained by VDCOM imaging when using a particular section of the EBSPs is strongly dependent on sample-detector geometry, surface topography, and beam energy (Nolze et al., 2017). This is outlined in the Results section where an explanation for the observed VDCOM images is given for the particular detector geometry, sample, and beam energy used in acquiring the N-polar GaN thin film dataset used in the present study.

Results

Virtual Diode Imaging

The virtual diode method was performed on the N-polar GaN sample by segmenting the screen into 20 rows and summing the signal in each row for each EBSP. Twenty rows were chosen in this case as they maximized the variation in contrast observed. Shown in Figure 4 are the VD images acquired from the top row (a) and the bottom row (b) of the N-polar GaN sample. The top and bottom rows demonstrate best the variation between VD images in terms of dominant contrast.

The virtual diode images initially showed dark horizontal lines, unrelated to crystallographic changes in the sample. This was potentially caused by either sample charging or fluctuation in the beam current. This was corrected by taking the median value of pixels across the dataset and subtracting the features common to all rows (horizontal lines). The corrected images are those shown in Figure 4, however, the “raw” virtual diode images can be seen in the [Supplementary Material](#), along with a more detailed description of the median correction.

Inspecting the VD image produced from the intensity distribution in the top row (Fig. 4a) shows that mainly dislocation contrast is observed, dots with black-white contrast on the sample surface. This is due to the same effect as discussed for ECCI previously, where changes in crystallographic orientation result in a change in the proximity of the incident beam

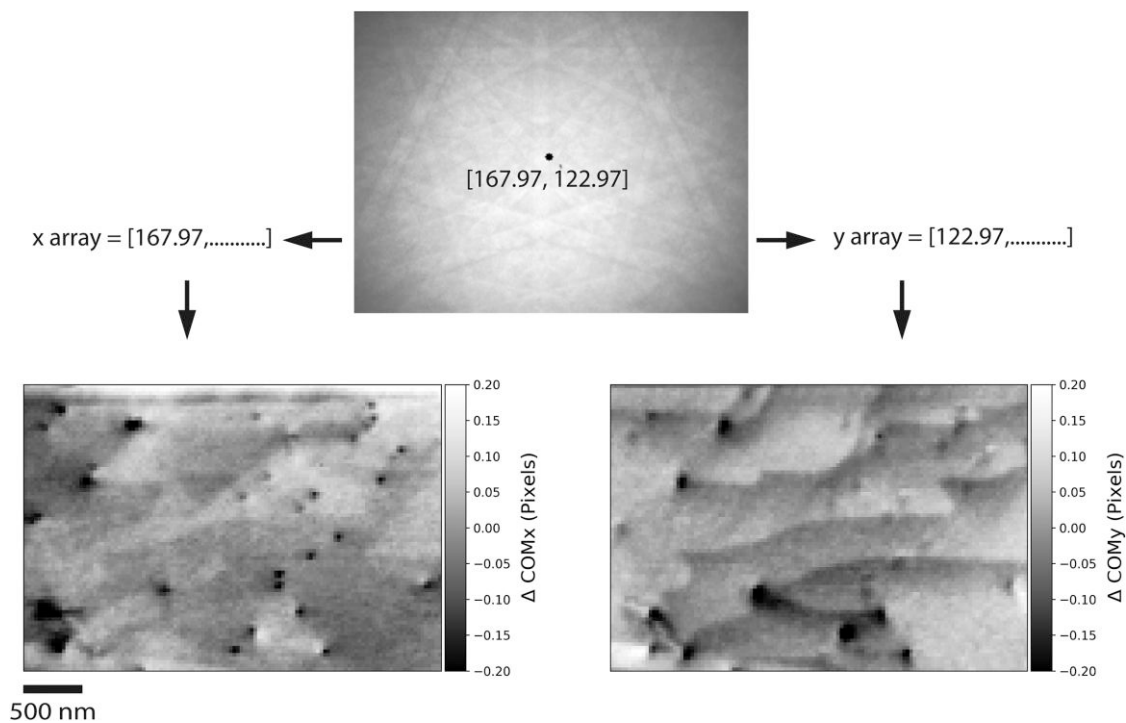


Fig. 3. COM imaging. The center of the intensity distribution of each EBSP is found for COM analysis and is marked by the dot in the example EBSP (top image). The x and y coordinates of the COM for every EBSP are plotted in two separate arrays and normalized by the mean value. These arrays are plotted giving COM x and COM y images, respectively. Note here there is no detector segmentation, the COM images are produced from the COM of the entire EBSP. The images shown are from the 900 nm thick N-polar GaN sample.

to the Bragg angle; meaning fewer or greater number of electrons are diffracted through the sample.

Figure 4b shows contrast which is dominated more by the surface steps on the sample. The dislocations which terminate these steps also show strong contrast as they are at the interface between the steps and the rest of the sample, while dislocations that do not terminate steps are fainter than in Figure 4a. The signal due to topography is now exceeding the signal due to changes in orientation of the crystal. To understand why this change in contrast occurs between the top and bottom row, we must consider the detector-sample geometry of the setup (Fig. 5a). With the sample inclined at 70° to the horizontal, the electrons incident on the bottom of the screen are at a grazing angle to the sample, making them more surface sensitive. These electrons are shadowed by the atomic steps, resulting in changes in the BSE yield.

Additionally, it can be seen in Figure 4 that the signal-to-noise in row 1/20 is less than that in row 20/20. This is also as a result of the geometry. As the sample is inclined, the volume of beam electrons within the sample (known as the interaction volume) is elongated in the sample y direction (Schwartz et al., 2009). As such, electrons will favor the forward direction when exiting the sample (Nolze et al., 2017), leading to an asymmetry in the BSE yield going down the detector screen. This can be confirmed by plotting a graph of the intensity recorded in each pixel row of the detector (Fig. 5b). This effect could be reduced by lowering the screen to increase electron incidence at the top of the screen and improve the signal, however as can be inferred from the shape of the distribution, this may mean less signal elsewhere on the screen.

Center of Mass Imaging

The following subsections “VDCOM y ” and “VDCOM x ” describe in detail the contrast exhibited from using VDCOM imaging on the N-polar GaN thin film sample.

The explanation for the contrast revealed in each image is particular to the sample-detector geometry, sample topography, and beam energy used in this research. The explanation cannot be applied for every instance of VDCOM imaging where one or more of these variables changes. Both VDCOM y and VDCOM x did not exhibit the horizontal lines the VD method did. This is because unwanted changes in the incoming beam current should not affect the position of the COM of the outgoing BSE distribution, highlighting an important advantage that COM imaging has over VD imaging.

VDCOM y

VDCOM y images were plotted by segmenting each EBSP into a top half and a bottom half. This gives two virtual diode regions per EBSP. The center of mass/intensity was then calculated as described previously for the top half and bottom half of the EBSPs separately. The deviation in the y position of each center of mass value from the mean was then plotted for both subsets of data, giving two images: VDCOM y from the top half of all EBSPs and VDCOM y from the bottom half of all EBSPs (Fig. 6).

Inspecting both VDCOM y images (Figs. 6a, 6b), we see that the signal produced is very similar to that in the VD images (Fig. 4). Again where there are dislocations, the BSE yield will vary and so the shape of the outgoing distribution will change. The direction in which the outgoing electrons are

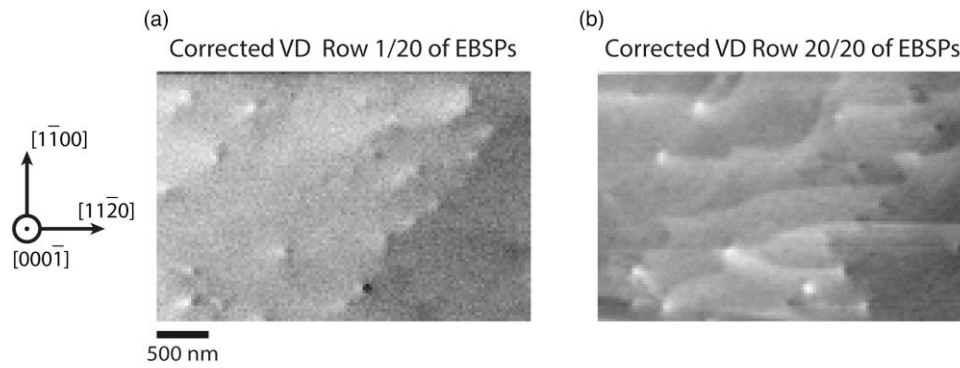


Fig. 4. (a) VD image produced from monitoring intensity changes in the top 5% of rows in EBSPs for N-polar GaN sample. (b) VD image produced from the bottom 5% of rows in EBSPs for N-polar GaN sample. These images have been corrected for unwanted signal changes via the application of a median function to the VD dataset (see [Supplementary Material](#)).

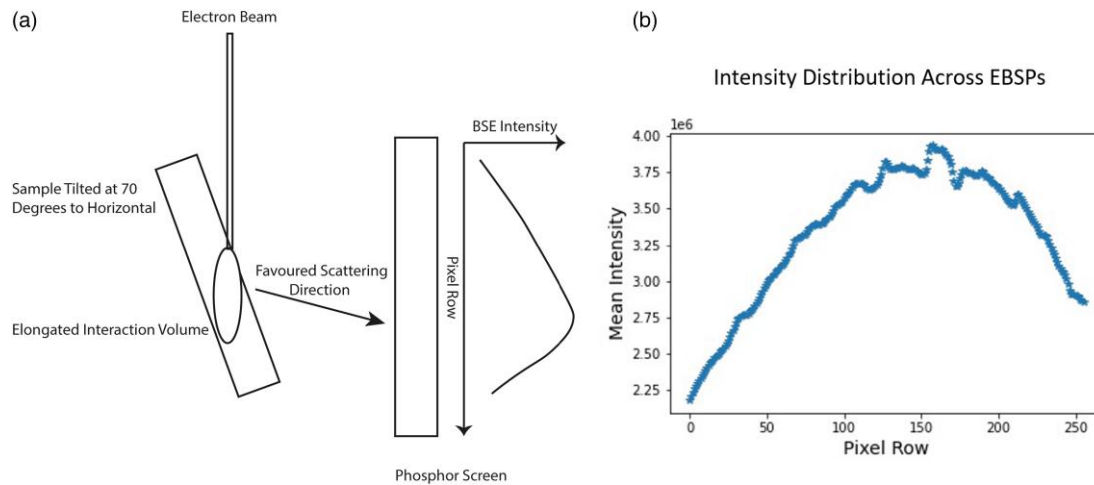


Fig. 5. (a) Effect of sample tilt on interaction volume is shown. Due to 70° tilt the interaction volume is elongated in the y direction resulting in an asymmetrical backscattered electron intensity distribution on the phosphor screen of the detector. This distribution shows the forward direction is favored by electrons exiting the sample surface. (b) Distribution of BSE signal from the first pixel row to the last on the detector.

scattered and diffracted will also change as the orientation of the crystal changes near dislocations. Both result in change in COM_y.

Furthermore, for the VDCOM_y produced from the bottom half of EBSPs, the image is formed from those electrons scattered at a grazing angle, meaning the contrast is particularly surface sensitive. When the beam scans in close proximity to steps, the electrons leaving the sample with grazing incidence will travel through a slightly greater depth to escape the sample. This results in a small shift in the y component of their backscattered direction, producing contrast in the resulting VDCOM_y image. Additionally, any shadowing due to surface steps may cause a change in the BSE distribution shape, and correspondingly a change in the COM_y position.

VDCOM_x

As with the VDCOM_y images, the VDCOM_x (Figs. 6c, 6d) images resulted from segmenting each EBSP into a top half and a bottom half.

There was significantly less variation in the dominant contrast mechanism for each VDCOM_x image. In fact, surface steps were largely absent. Additionally, many of the dislocations were resolved as smaller dots, in contrast to the spots with clear black–white contrast in the VDCOM_y images.

This made it easier to discern the number of dislocations present in the sample area, as some dislocations are very close to one another. The contrast is consistent with expectations, as COM_x analysis is generally less sensitive to topography (Winkelmann et al., 2017). In the case of the surface steps observed in the sample and geometry used, the absence of surface steps in VDCOM_x could possibly be explained by the fact that changes in the position of the BSE distribution in the x direction occur only due to shadowing. This is not the case for VDCOM_y where changes in the COM_y position occur due to the fact that electrons with grazing incidence are backscattered in the y direction slightly more when exiting near a step.

VD and VDCOM Suitability for Dislocation Imaging

When inspecting the quality of images produced by VD and VDCOM methods, their suitability for imaging dislocation distributions in nitride thin films can be assessed. For the VD method, we are only able to produce images showing only dislocations by placing the virtual diode at the top of the screen for this particular experimental setup (Fig. 4a). Due to the sample detector geometry, this means that unfortunately, signal-to-noise is poor in these images, resulting in a fairly low-quality image of the dislocation distribution. While the detector screen could physically be moved inside

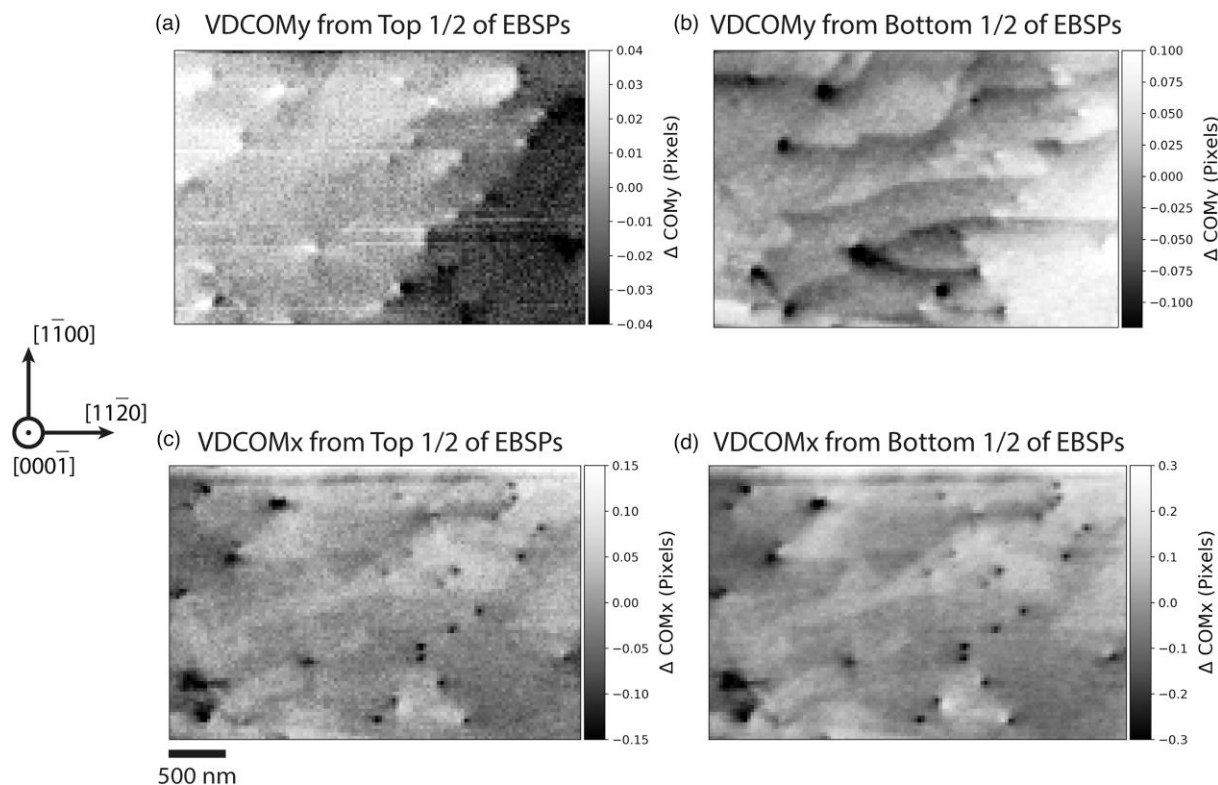


Fig. 6. VDCOMy image produced from the (a) top half and (b) bottom half of EBSPs in the N-polar GaN dataset. VDCOMx image produced from the (c) top half and (d) bottom half of EBSPs in the N-polar GaN dataset.

the SEM chamber to improve the signal-to-noise at the top of the screen, the asymmetry of the BSE distribution would mean there would be less signal at the bottom of the screen, deteriorating the surface step images. This however is not an issue with VDCOM imaging, as the insensitivity to surface steps that VDCOMx exhibits here means that we obtain images from the bottom of the screen with high signal and high dislocation contrast, while reducing the effect of topography (Fig. 6c). The dislocations also appear as small black dots, making them easily resolvable from one another, as opposed to the strong black-white contrast in the VD image showing just dislocations. While this shows a clear advantage of using VDCOM over VD, VD does have greater versatility in that VD images can be formed from small areas of the detector. This means there is greater flexibility in where we can place the virtual diode when we are just monitoring intensity changes, compared to monitoring the change in position of the distribution, which requires a large enough area that these changes are detectable. However, for this particular case, VDCOM is clearly superior to VD imaging in the range and quality of images it can produce.

VDCOM Applicability for Other Nitride Thin Films

Here, we show the applicability of VDCOM across three other nitride thin films, exhibiting a range of dislocation densities. Figures 7a–7c show VDCOMy images produced from the bottom half of EBSPs for two different Ga-polar GaN thin films and an AlN thin film, respectively. VDCOMy images were chosen as they exhibit contrast from both steps and dislocations in these samples. The dislocation densities are $3 \times 10^8 \text{ cm}^{-2}$, $2 \times 10^9 \text{ cm}^{-2}$, and $1 \times 10^9 \text{ cm}^{-2}$ for (a), (b), and (c), respectively. For comparison, the dislocation density

for the N-polar GaN sample discussed earlier is of the order of $1 \times 10^8 \text{ cm}^{-2}$.

Inspecting the images for the two GaN films (Figs. 7a, 7b), we can begin to understand the limitations on imaging GaN thin films with the VDCOM technique. Surface steps can easily be identified in Figure 7a, although where they terminate is less clear than that in Figure 6b, meanwhile individual dislocations are completely resolved. However, as the dislocation and step densities increase again going to the Ga-polar GaN sample shown in Figure 7b, it becomes much harder to resolve individual steps, although it is still clear that they are present. Here, dislocations are still just as prominent as in Figures 7a and 6b, and there is even strong subgrain contrast where subgrains are decorated by the dislocation distribution. The strong dislocation and weak step contrast occurs in the higher density samples because as the step density increases, steps are more difficult to fully resolve and their effect on the intensity distribution is averaged out, allowing the dislocation contrast to stay dominant.

This effect is also apparent when moving to other materials such as AlN thin films (Fig. 7c). This sample exhibits a relatively high dislocation density ($1 \times 10^9 \text{ cm}^{-2}$) and surface step density. The individual dislocations are still fully resolvable, while the surface step contrast is significantly decreased.

While it is unfortunate that individual steps and where they terminate cannot be fully resolved in the samples shown in Figure 7, it highlights an important limitation of the imaging technique. As the step density approaches the spatial resolution of EBSD, the ability to both resolve surface steps and determine where they terminate significantly decreases. Improving spatial resolution, and therefore further optimizing VDCOM imaging by going to lower beam voltages is the subject of ongoing research.

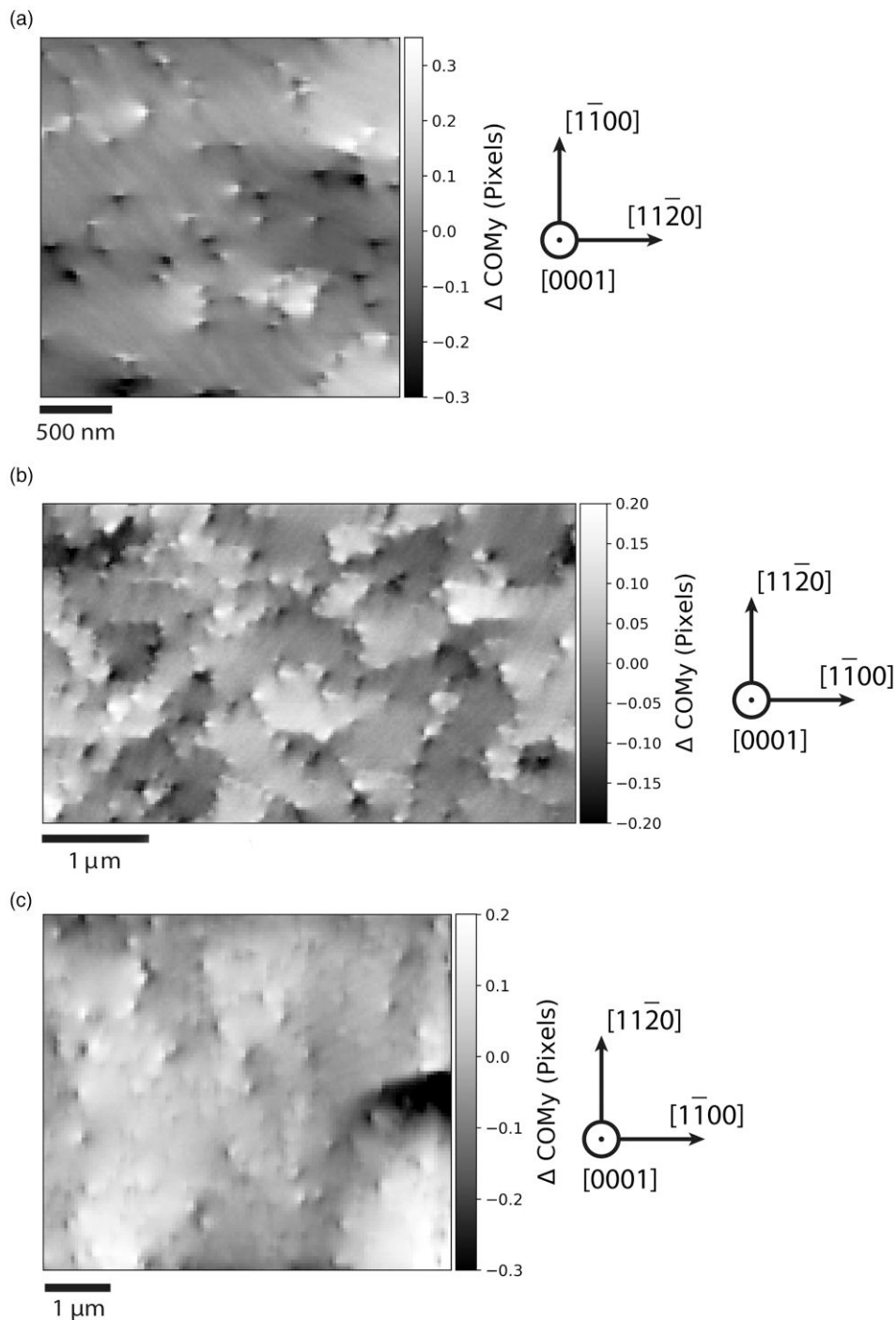


Fig. 7. VDCOMy images produced from bottom half of EBSPs from a **(a)** 1600 nm thick Ga-polar GaN thin film with a dislocation density of $3 \times 10^8 \text{ cm}^{-2}$, **(b)** 2150 nm thick Ga-polar GaN thin film with a dislocation density of $2 \times 10^9 \text{ cm}^{-2}$, and **(c)** $6.6 \mu\text{m}$ thick AlN thin film with a dislocation density of $1 \times 10^9 \text{ cm}^{-2}$.

Ultimately, here, we demonstrate that VDCOMy imaging is still a useful method for imaging individual dislocations and dislocation distributions at relatively high dislocation densities in nitride thin films, while surface steps become more difficult to resolve for higher step densities.

Conclusion

The use of a pixelated detector for nitride thin film imaging allows greater flexibility than the hardware diodes that have traditionally been used in SEM based dislocation imaging. By

using a pixelated detector the user can define multiple “virtual” diodes of different shapes and sizes which can be located in any position across the pixel array. By monitoring how the total intensity recorded in these virtual diodes changes as the beam moves across the sample, different images of the same sample surface can be produced showing different dominant contrast mechanisms. In this particular study, we have shown how we can controllably produce surface images of an N-polar GaN thin film using the VD method which show either dislocations or surface steps and dislocations.

Another advantage of using a pixelated detector is that the change in position of the recorded BSE distribution can also be monitored as the electron beam is scanned across the sample (known as center of mass imaging). Here, we have shown that by applying COM imaging within virtual diodes (VDCOM imaging), we can again control the type of contrast dominating the images produced by this technique; showing either dislocations or surface steps and dislocations. VDCOM has the advantage over regular (full EBSP) COM imaging in that it has the potential to offer better refinement of the type of image contrast obtained (topography, dislocations, etc.). This can be particularly helpful when contrast from one type of feature is highly suppressed in the original COM image. Here, the placement of virtual diodes and resulting VDCOM analysis can improve this contrast by measuring the COM shift in parts of the EBSPs where the BSE contribution from the other, more dominant effect, should be less.

We have demonstrated that VDCOM produces images of both dislocations and dislocations and surface steps with high signal-to-noise, by utilizing the fact we can monitor changes in the backscattered electron intensity distribution in both the x and y positions. Meanwhile, VD imaging can also produce images of dislocations or dislocations and surface steps, but due to the asymmetry of the intensity distribution across the detector screen, one image will inevitably have a poorer signal-to-noise ratio. While this is advantageous for the VDCOM technique, VD imaging is more flexible in that the virtual diodes can be significantly smaller when measuring the change in the magnitude of the BSE yield than when measuring changes in the position of the BSE distribution. This is purely because as smaller virtual diodes are used for VDCOM, the area over which changes in the COM are detectable is much smaller, reducing the signal-to-noise in the resulting VDCOM images. VDCOM is, however, also unaffected by unwanted modulations in beam current or charging, as demonstrated with the N-polar GaN dataset used here, whereas VD imaging suffers from this.

Ultimately, from the data sampled here, it is suggested that for dislocation analysis, VDCOM imaging provides the best images in that different features can be emphasized and the resulting images have high signal-to-noise.

Finally, we have illustrated the applicability of VDCOM as an imaging technique across other thin film samples with varying surface step densities and dislocation densities. It is clear that at high surface step densities it no longer becomes possible to identify where surface steps terminate, although they are still visible. Despite this, at higher dislocation densities, VDCOM is still able to resolve individual dislocations and images exhibit sub-grain contrast. This provides valuable information on dislocation distributions on the surface of nitride thin film samples.

Availability of Data and Materials

The experimental data presented in this article is available at <https://doi.org/10.15129/318a308b-13f6-4e0e-a3e6-4c69e7e70da1> or from the corresponding author.

Supplementary Material

To view supplementary material for this article, please visit <https://doi.org/10.1093/micmic/ozad118>.

Acknowledgments

The authors have no acknowledgements.

Financial Support

This work was carried out with the support of UK EPSRC projects EP/P015719/1 and EP/T012692/1. J.B. would like to thank the Royal Society of Edinburgh (RSE) for a Saltire International Collaboration Award (1917). A.W. was supported by the Polish National Science Centre (NCN), grant number 2020/37/B/ST5/03669.

Conflict of Interest

No conflict of interest is declared.

References

- Bojarska-Cieślińska A, Marona L, Smalc-Koziorowska J, Grzanka S, Weyher J, Schiavon D & Perlin P (2021). Role of dislocations in nitride laser diodes with different indium content. *Sci Rep* **11**, 21. <https://doi.org/10.1038/s41598-020-79528-z>
- Brodusch N, Demers H & Gauvin R (2015). Dark-field imaging based on post-processed electron backscatter diffraction patterns of bulk crystalline materials in a scanning electron microscope. *Ultramicroscopy* **148**, 123–131. <https://doi.org/10.1016/j.ultramic.2014.09.005>
- Brodusch N, Demers H & Gauvin R (2018a). Imaging with a commercial electron backscatter diffraction (EBSD) camera in a scanning electron microscope: A review. *J Imaging* **4**, 88. <https://doi.org/10.3390/jimaging4070088>
- Brodusch N, Demers H & Gauvin R (2018b). Electron diffraction techniques in the SEM. In *Field Emission Scanning Electron Microscopy*. Springer Briefs in Applied Sciences and Technology, pp. 85–105. Singapore: Springer.
- Callahan PG, Haidet BB, Jung D, Seward GGE & Mukherjee K (2018). Direct observation of recombination-enhanced dislocation glide in heteroepitaxial GaAs on silicon. *Phys Rev Mater* **2**, 081601. <https://doi.org/10.1103/PhysRevMaterials.2.081601>
- Carnevale SD, Deitz JI, Carlin JA, Picard YN, De Graef M, Ringel SA & Grassman TJ (2014). Rapid misfit dislocation characterization in heteroepitaxial III-V/Si thin films by electron channeling contrast imaging. *Appl Phys Lett* **104**, 232111. <https://doi.org/10.1063/1.4883371>
- Chapman M, Callahan PG & De Graef M (2016). Determination of sample surface topography using electron back-scatter diffraction patterns. *Scr Mater* **120**, 23–26. <https://doi.org/10.1016/j.scriptamat.2016.03.032>
- Crimp MA, Simkin BA & Ng BC (2001). Demonstration of the $g \cdot b \times u = 0$ edge dislocation invisibility criterion for electron channelling contrast imaging. *Philos Mag Lett* **81**, 833–837. <https://doi.org/10.1080/09500830110088755>
- Han H, Hantschel T, Strakos L, Vystavel T, Baryshnikova M, Mols Y, Kunert B, Langer R, Vandervorst W & Caymax M (2020). Application of electron channeling contrast imaging to 3D semiconductor structures through proper detector configurations. *Ultramicroscopy* **210**, 112928. <https://doi.org/10.1016/j.ultramic.2019.112928>
- Hite J, Mastro M & Eddy C (2010). Approach for dislocation free GaN epitaxy. *J Cryst Growth* **312**, 3143. <https://doi.org/10.1016/j.jcrysgro.2010.07.054>
- Hull D & Bacon DJ (2011). *Introduction to Dislocations*. Oxford: Butterworth-Heinemann.
- Kaboli S & Burnley PC (2018). Direct observations of crystal defects in polycrystalline diamond. *Mater Charact* **142**, 154–161. <https://doi.org/10.1016/j.matchar.2018.05.036>
- Kneissl M, Seong T-Y, Han J & Amano H (2019). The emergence and prospects of deep-ultraviolet light-emitting diode technologies. *Nat Photonics* **13**, 233–244. <https://doi.org/10.1038/s41566-019-0359-9>
- Lafford TA, Parbrook PJ & Tanner BK (2002). Direct, independent measurement of twist and tilt mosaic as a function of thickness in epitaxial GaN. *Phys Status Solidi C: Conf* **545**, 542. <https://doi.org/10.1002/pssc.200390109>

- Lähmann J, Kaganer VM, Sabelfeld KK, Kireeva AE, Jahn U, Chèze C, Calarco R & Brandt O (2022). Carrier diffusion in GaN: A cathodoluminescence study. III. Nature of nonradiative recombination at threading dislocations. *Phys Rev Appl* 17, 024019. <https://doi.org/10.1103/PhysRevApplied.17.024019>
- L'hôte G, Lafond C, Steyer P, Deschanel S, Douillard T, Langlois C & Cazottes S (2019). Rotational-electron channeling contrast imaging analysis of dislocation structure in fatigued copper single crystal. *Scr Mater* 162, 103–107. <https://doi.org/10.1016/j.scriptamat.2018.10.050>
- Mathis SK, Romanov AE, Chen LF, Beltz GE, Pompe W & Speck JS (2001). Modeling of threading dislocation reduction in growing GaN layers. *J Cryst Growth* 231, 371. [https://doi.org/10.1016/S0022-0248\(01\)01468-3](https://doi.org/10.1016/S0022-0248(01)01468-3)
- Miyajima N, Li Y, Abeykoon S & Heidelbach F (2018). Electron channeling contrast imaging of individual dislocations in geological materials using a field-emission scanning electron microscope equipped with an EBSD system. *Eur J Mineral* 30, 5–15. <https://doi.org/10.1127/ejm/2017/0029-2683>
- Nagahama S, Iwasa N, Senoh M, Matsushita T, Sugimoto Y, Kiyoku H, Kozaki T, Sano M, Matsumura H, Umemoto H, Chocho K, Yanamoto T & Mukai T (2001). GaN-based light-emitting diodes and laser diodes, and their recent progress. *Phys Status Solidi (A) Appl Res* 188, 1. [https://doi.org/10.1002/\(ISSN\)1521-396X](https://doi.org/10.1002/(ISSN)1521-396X)
- Naresh-Kumar G, Hourahine B, Edwards PR, Day AP, Winkelmann A, Wilkinson AJ, Parbrook PJ, England G & Trager-Cowan C (2012). Rapid nondestructive analysis of threading dislocations in wurtzite materials using the scanning electron microscope. *Phys Rev Lett* 108, 135503. <https://doi.org/10.1103/PhysRevLett.108.135503>
- Nolze G, Hielscher R & Winkelmann A (2017). Electron backscatter diffraction beyond the mainstream. *Cryst Res Technol* 52, 1600252. <https://doi.org/10.1002/crat.201600252>
- Nowell MM, Wright SI, Rampton T & de Kloer R (2014). Advances in scattered electron intensity distribution imaging for microstructural visualization and correlations with EBSD measurements. *Microsc Microanal* 20, 856. <https://doi.org/10.1017/S143192761400600X>
- Picard YN, Kamaladasa R, De Graef M, Nuhfer NT, Mershon WJ, Owens T, Sedlacek L & L'opour F (2012). Future prospects for defect and strain analysis in the SEM via electron channeling. *Microsc Today* 20, 12–16. <https://doi.org/10.1017/S1551929512000077>
- Rampton TM, Nowell MM & Wright SI (2014). New tools for the study of deformed and heat-treated materials via electron backscatter diffraction. *Microsc Microanal* 20, 1482. <https://doi.org/10.1017/S1431927614009143>
- Schulze A, Strakos L, Vystavel T, Loo R, Pacco A, Collaert N, Vandervorst W & Caymax M (2018). Non-destructive characterization of extended crystalline defects in confined semiconductor device structures. *Nanoscale* 10, 7058–7066. <https://doi.org/10.1039/C8NR00186C>
- Schwartz AJ, Kumar M, Adams BL & Field DP (Eds.) (2009). *Electron Backscatter Diffraction in Materials Science*. NY: Springer.
- Schwarzer RA & Sukkau J (2013). Electron back scattered diffraction: Current state, prospects and comparison with X-ray diffraction texture measurement. *Banaras Metall* 18, 1. https://scholar.google.com/scholar_lookup?title=Electron+back+scattered+diffraction:+Current+state,+prospects+and+comparison+with+X-ray+diffraction+texture+measurement&author=Schwarzer,+R.A.&author=Sukkau,+J.&publication_year=2013&journal=Banaras+Metall.&volume=18&pages=1%E2%80%9311
- Setera B & Christou A (2021). Threading dislocations in GaN high-voltage switches. *Microelectron Reliab* 124, 114336. <https://doi.org/10.1016/j.microrel.2021.114336>
- Tanaka T, Kawakami K, Mogi H & Arai S (2023). An EBSD camera as a tool to characterise in-plane magnetisation vectors on Fe–Si (001) surface. *Ultramicroscopy* 250, 113754. <https://doi.org/10.1016/j.ultramic.2023.113754>
- Trager-Cowan C, Sweeney F, Trimby PW, Day AP, Gholinia A, Schmidt NH, Parbrook PJ, Wilkinson AJ & Watson IM (2007). Electron backscatter diffraction and electron channeling contrast imaging of tilt and dislocations in nitride thin films. *Phys Rev B* 75, 085301. <https://doi.org/10.1103/PhysRevB.75.085301>
- Vilalta-Clemente A, Naresh-Kumar G, Nouf-Allahiani M, Gamarra P, di Forte-Poisson MA, Trager-Cowan C & Wilkinson AJ (2017). Cross-correlation based high resolution electron backscatter diffraction and electron channeling contrast imaging for strain mapping and dislocation distributions in InAlN thin films. *Acta Mater* 125, 125–135. <https://doi.org/10.1016/j.actamat.2016.11.039>
- Walde S, Hagedorn S, Coulon PM, Mogilatenko A, Netzel C, Weinrich J, Susilo N, Ziffer E, Matiwe L, Hartmann C, Kusch G, Alasmari A, Naresh-Kumar G, Trager-Cowan C, Wernicke T, Straubinger T, Bickermann M, Martin RW, Shields PA, Kneissl M & Weyers M (2020). AlN overgrowth of nano-pillar-patterned sapphire with different offcut angle by metalorganic vapor phase epitaxy. *J Cryst Growth* 531, 125343. <https://doi.org/10.1016/j.jcrysgro.2019.125343>
- Weisbuch C (2019). Review—On the search for efficient solid state light emitters: Past, present, future. *ECS J Solid State Sci Technol* 9, 016022. <https://doi.org/10.1149/2.0392001JSS>
- Wells OC, Savoy RJ, Bailey PJ, Wells OC, Savoy RJ & Bailey PJ (1982). Backscattered electron (BSE) imaging in the scanning electron microscope (SEM) - measurement of surface layer mass-thickness. *Scan Electron Microsc* 1982, 25. <https://digitalcommons.usu.edu/electron/vol1982/iss1/25/>
- Wilkinson AJ & Hirsch PB (1997). Electron diffraction based techniques in scanning electron microscopy of bulk materials. *Micron* 28, 279–308. [https://doi.org/10.1016/S0968-4328\(97\)00032-2](https://doi.org/10.1016/S0968-4328(97)00032-2)
- Winkelmann A (2017). Model mechanisms in Kikuchi pattern formation from crystals. *Cryst Res Technol* 52, 1600288. <https://doi.org/10.1002/crat.v52.4>
- Winkelmann A, Britton TB & Nolze G (2019). Constraints on the effective electron energy spectrum in backscatter Kikuchi diffraction. *Phys Rev B* 99, 064115. <https://doi.org/10.1103/PhysRevB.99.064115>
- Winkelmann A, Cios G, Tokarski T, Bala P, Grin Y & Burkhardt U (2023). Assignment of chiral elemental crystal structures using Kikuchi diffraction. *Mater Charact* 196, 112633. <https://doi.org/10.1016/j.matchar.2022.112633>
- Winkelmann A, Nolze G, Vespucci S, Naresh-Kumar G, Trager-Cowan C, Vilalta-Clemente A, Wilkinson AJ & Vos M (2017). Diffraction effects and inelastic electron transport in angle-resolved microscopic imaging applications. *J Microsc* 267, 330. <https://doi.org/10.1111/jmi.2017.267.issue-3>
- Winkelmann A & Vos M (2013). The role of localized recoil in the formation of Kikuchi patterns. *Ultramicroscopy* 125, 66–71. <https://doi.org/10.1016/j.ultramic.2012.11.001>
- Wright SI, Nowell MM, De Kloer R, Camus P & Rampton T (2015). Electron imaging with an EBSD detector. *Ultramicroscopy* 148, 132–145. <https://doi.org/10.1016/j.ultramic.2014.10.002>
- Wu XH, Brown LM, Kapolnek D, Keller S, Keller B, DenBaars SP & Speck JS (1996). Defect structure of metal-organic chemical vapor deposition-grown epitaxial (0001) GaN/Al₂O₃. *J Appl Phys* 80, 3228–3237. <https://doi.org/10.1063/1.363264>
- Yaung KN, Kirnstoetter S, Faucher J, Gerger A, Lochtefeld A, Barnett A & Lee ML (2016). Threading dislocation density characterization in III–V photovoltaic materials by electron channeling contrast imaging. *J Cryst Growth* 453, 65. <https://doi.org/10.1016/j.jcrysgro.2016.08.015>
- Zaefferer S & Elhami NN (2014). Theory and application of electron channeling contrast imaging under controlled diffraction conditions. *Acta Mater* 75, 20–50. <https://doi.org/10.1016/j.actamat.2014.04.018>